PARP1 inhibitors trigger innate immunity via PARP1 trapping-induced DNA damage response

Chiho Kim, Xu-Dong Wang, Yonghao Yu*

Department of Biochemistry, University of Texas Southwestern Medical Center, Dallas, United States

Abstract It is being increasingly appreciated that the immunomodulatory functions of PARP1 inhibitors (PARPi) underlie their clinical activities in various *BRCA*-mutated tumors. PARPi possess both PARP1 inhibition and PARP1 trapping activities. The relative contribution of these two mechanisms toward PARPi-induced innate immune signaling, however, is poorly understood. We find that the presence of the PARP1 protein with uncompromised DNA-binding activities is required for PARPi-induced innate immune response. The activation of cGAS-STING signaling induced by various PARPi closely depends on their PARP1 trapping activities. Finally, we show that a small molecule PARP1 degrader blocks the enzymatic activity of PARP1 without eliciting PARP1 trapping or cGAS-STING activation. Our findings thus identify PARP1 trapping as a major contributor of the immunomodulatory functions of PARPi. Although PARPi-induced innate immunity is highly desirable in human malignancies, the ability of 'non-trapping' PARP1 degraders to avoid the activation of innate immune response could be useful in non-oncological diseases.

Introduction

Poly-ADP-ribose polymerase 1 (hereafter referred to as PARP1) is an enzyme that is critically involved in mediating DNA damage response (DDR). Upon sensing the genotoxic stress, PARP1 is recruited to DNA stand breaks and is activated to synthesize negatively charged Poly-ADP-ribose (PAR) polymers. One of the functions of these PAR chains is to serve as a platform to recruit the DDR machinery to repair and resolve these DNA breaks (*Ray Chaudhuri and Nussenzweig, 2017*; *Gibson and Kraus, 2012*). Therapeutics that target PARP1 have been proposed as an attractive strategy to treat human malignancies. Indeed, cancers with *BRCA1/2* mutations rely on PARP1 for genome integrity, and they are selectively killed by PARP1 inhibitors (PARPi) via the 'synthetic lethality' mechanism (*Lord et al., 2015*; *Lord and Ashworth, 2017*; *Farmer et al., 2005*). Four PARPi (Olaparib, Rucaparib, Niraparib, and Talazoparib) have been approved by the FDA to treat *BRCA1/2*-deficient breast and/or ovarian cancers (*Faraoni and Graziani, 2018*). In addition, PARPi are being extensively evaluated in the clinic, either as single agents or in combination with chemo- and radiation-therapy approaches, for the treatment of many other solid tumors (*Rouleau et al., 2010*; *Lord and Ashworth, 2017*).

All FDA-approved PARPi are NAD^+-competitive, and it was initially thought that these agents kill tumors simply by inhibiting the catalytic activity of PARP1. However, recent studies suggest that the cytotoxicity of PARPi is ascribed, at least in part, to the ability of these compounds to induce PARP1 trapping (*Hopkins et al., 2019*; *Murai et al., 2012*). During DDR, PARP1 is activated to catalyze the Poly-ADP-ribosylation (PARylation) of many proteins, including PARP1 itself. PARylation triggers the release of PARP1 from the DNA lesions, owing to the charge repulsion and steric hindrance introduced by the PAR polymers. PARPi block the synthesis of PAR chains, which causes PARP1 to be trapped on the chromatin. The trapped PARP1 triggers further DNA damage, cell cycle arrest, and

eventually, cancer cell death (*Lord and Ashworth, 2017*; *Slade, 2020*). Besides the PARylation-dependent mechanism, several recent studies also suggest that although the various clinically relevant PARPi all bind to PARP1, they induce different degrees of PARP1 conformational changes, and in doing so, PARP1 trapping (*Lord and Ashworth, 2017*; *Hopkins et al., 2019*; *Murai et al., 2014*; *Shen et al., 2013*; *Murai et al., 2012*).

Many recent studies have provided compelling evidence for a functional link between tumor DNA damage and the immune system, during the treatment of cancers. During chemo- and radiation-therapy, self-DNA is released, and is detected by the cytosolic DNA sensor, cyclic GMP-AMP (cGAMP) synthetase (cGAS). cGAS subsequently produces the second messenger cGAMP. cGAMP binds to Stimulator of Interferon Genes (STING), leading to the recruitment and activation of Tank-binding kinase I (TBK1). TBK1 phosphorylates a transcription factor called interferon regulatory factor 3 (IRF3), resulting in its nuclear translocation, and the IRF3-dependent activation of type I interferon (IFN) signaling (*Chen et al., 2016*; *Ishikawa and Barber, 2008*; *Li and Chen, 2018*; *Barber, 2015*). Thus, the cGAS-STING pathway plays a vital role not only in protecting the cells against a variety of pathogens, but also in the antitumor immune response. Because PARPi treatment is known to produce cytosolic dsDNA (double-stranded DNA), it has been proposed that the activation of innate immune signaling could be a critical molecular mechanism underlying the therapeutic effect of PARPi (*Ding et al., 2018*; *Shen et al., 2019*; *Pantelidou et al., 2019*; *Sen et al., 2019*). However, the relative contribution of the two independent, yet interconnected mechanisms (i.e., PARP1 inhibition and PARP1 trapping) in mediating the antitumor immunity of PARPi is not well understood.

In this study, we show that PARPi treatment induces the antitumor immune response via the cGAS-STING pathway. However, PARPi treatment generates cytosolic dsDNA, only in the presence of the PARP1 protein. PARPi-induced dsDNA is subsequently recognized by cGAS, which leads to the activation of innate immune signaling. We subsequently employed a series of clinically relevant PARPi with different PARP1 trapping activities, as well as a 'non-trapping' PARP1 degrader. We showed that the activation of innate immune signaling is critically dependent on the PARP1 trapping activity of these compounds. These results provide evidence that PARPi-mediated PARP1 trapping, but not the catalytic inhibition of PARP1, is a key determinant for the activation of the innate immune response.

Results

PARPi activates innate immune signaling via the cGAS-STING pathway

It is being increasingly appreciated that chemo- and radiation-therapy cause the formation of cytosolic dsDNA and micronuclei, which, in turn, lead to the activation of the cGAS-STING signaling pathway and inflammatory responses in tumors (*Vanpouille-Box et al., 2018*; *Liang and Peng, 2016*; *Harding et al., 2017*; *Mackenzie et al., 2017*; *Dou et al., 2017*; *Glück et al., 2017*; *Vanpouille-Box et al., 2017*; *Yum et al., 2019*). We explored the immunomodulatory functions of PARPi using Talazoparib, which is an FDA-approved PARP1 inhibitor that is known to potently inhibit and trap PARP1 (*Figure 1A*). We found that Talazoparib treatment was able to induce the formation of cytosolic dsDNA (*Figure 1B*) as well as γH2AX (a marker for DNA double strand breaks) (*Figure 1C*). To evaluate the innate immune response, we examined the phosphorylation of TBK1 (pS172 TBK1) and IRF3 (pS396 IRF3), two critical components in the cGAS-STING pathway (*Motwani et al., 2019*; *Kato et al., 2017*). Indeed, Talazoparib treatment dramatically increased both phosphorylation events (*Figure 1D and E*). Talazoparib treatment also remarkably induced the nuclear translocation of phospho-IRF3 (*Figure 1E*, right), which is a critical step for IRF3-mediated gene transcription (*Kato et al., 2017*; *Motwani et al., 2019*). We then examined the mRNA expression level of a number of known downstream target genes of the cGAS-STING pathway. Consistent with the previous studies (*Sun et al., 2013*; *Parkes et al., 2017*; *Fu et al., 2020*), Talazoparib treatment greatly upregulated the expression of type I interferons (IFN; *Inf-α* and *Inf-β*), pro-inflammatory cytokines (*Ccl5* and *Cxcl10*), and interferon-stimulated genes (ISGs; *Isg15*, *Mx1*, *Mx2*, and *Ifit3*) (*Figure 1F*, *Figure 1—figure supplement 1A*). To examine whether the cGAS-STING pathway is necessary for the PARPi-induced innate immune signaling, we depleted cGAS using two independent short hairpin RNAs (shRNAs) (*Figure 1G*). Knock-down (KD) of cGAS did not interfere with PARP1 trapping
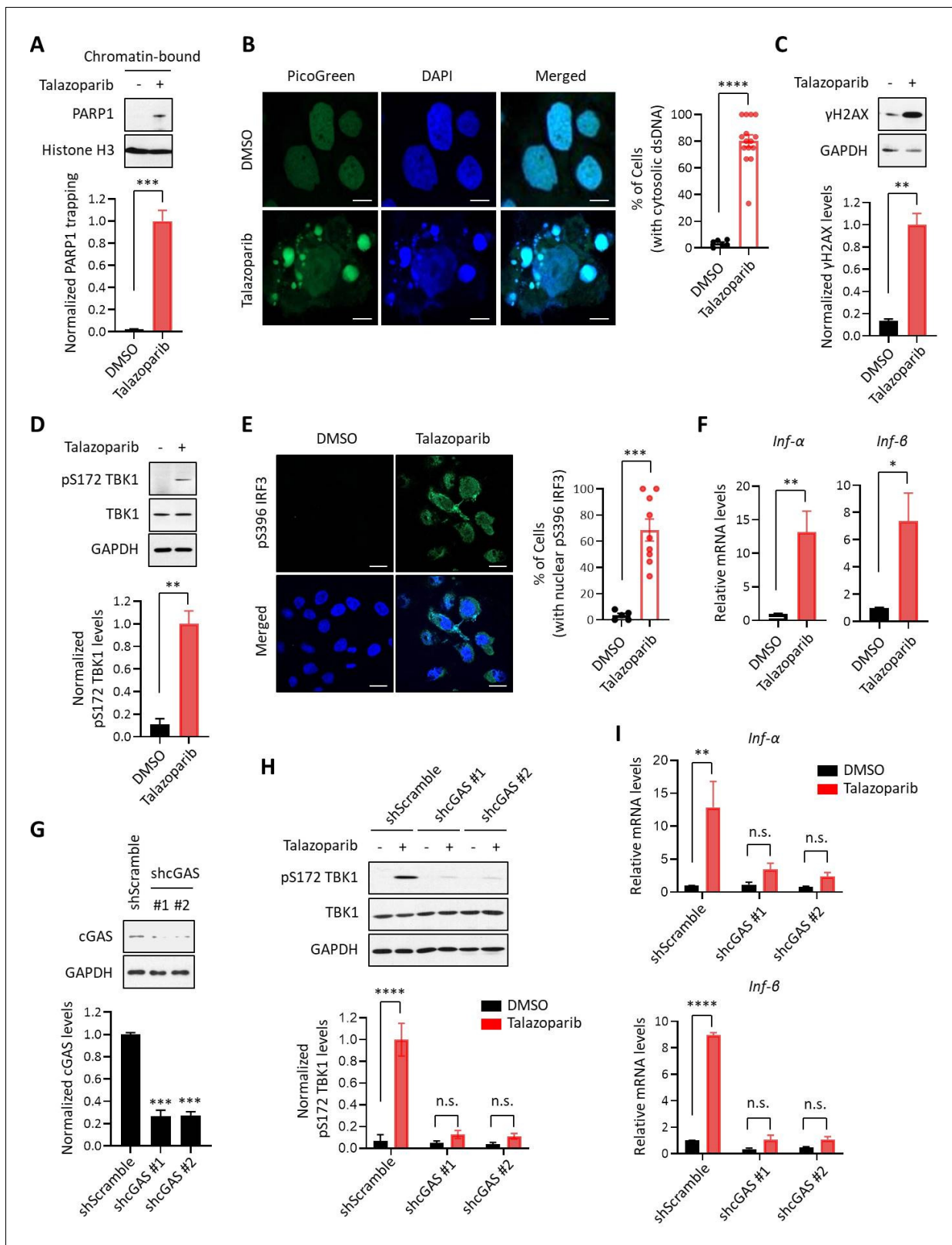
Figure 1. PARPi induces the innate immune response via the cGAS-STING pathway. (**A**) The level of trapped PARP1 in HeLa cells treated with or without Talazoparib (10 μM for 72 hr). Top, chromatin-bound fractions were isolated and were probed using the indicated antibodies. Histone H3 was used as the loading control. Bottom, the graph shows the quantification of the level of PARP1 trapping. Values were presented as means ± SD from three biological replicates. Significance was determined with unpaired Student's t-test. ***p < 0.001. (**B**) Staining of cytosolic dsDNA in HeLa cells

Figure 1 continued on next page

Figure 1 continued

treated with or without Talazoparib (10 µM for 72 hr). Left, representative image of PicoGreen (green) staining. DAPI (blue) was used to visualize the nucleus. Scale bars represent 10 µm. Right, the graph shows the quantification of the number of cells with cytosolic dsDNA. Values were presented as means ± SEM from three biological replicates (n = 3 fields,≥100 cells counted per condition). Significance was determined with unpaired Student's t-test. ****p < 0.0001. (**C**) The extent of DNA damage in HeLa cells treated with or without Talazoparib (10 µM for 72 hr). Top, whole cell lysates were probed using the indicated antibodies. Bottom, the graph shows the quantification of γH2AX levels. Values were presented as means ± SD from three biological replicates. Significance was determined with unpaired Student's t-test. **p < 0.01. (**D**) The level of pS172 TBK1 in HeLa cells treated with or without Talazoparib (10 µM for 72 hr). Top, whole cell lysates were probed using the indicated antibodies. Bottom, the graph shows the quantification of pS172 TBK1 levels. Values were presented as means ± SD from three biological replicates. Significance was determined with unpaired Student's t-test. **p < 0.01. (**E**) The level of pS396 IRF3 in HeLa cells treated with or without Talazoparib (10 µM for 72 hr). Left, representative image of pS396 IRF3 levels (green). DAPI (blue) was used to visualize the nucleus. Scale bars represent 20 µm. Right, the graph shows the quantification of the number of cells stained positive for pS396 IRF3 in nucleus. Values were presented as means ± SEM from three biological replicates (n = 3 fields,≥100 cells counted per condition). Significance was determined with unpaired Student's t-test. ***p < 0.001. (**F**) RT-qPCR of type I interferons levels in HeLa cells treated with or without Talazoparib (10 µM for 72 hr). Values of *Inf-α* and *Inf-β* were presented as means ± SEM from three biological replicates. Significance was determined with unpaired Student's t-test. *p < 0.05, **p < 0.01. (**G**) Knock-down of cGAS. HeLa cells expressing the control shRNA (shScramble) or shcGAS (shcGAS #1 or #2) were probed using the indicated antibodies. Right, the graph shows the ratio of cGAS depletion. Values were presented as means ± SD from three biological replicates. Significance was determined with one-way ANOVA. ***p < 0.001. (**H**) Depletion of cGAS abolishes PARPi-induced activation of innate immune signaling. HeLa cells expressing shRNA against control (shScramble) or cGAS (shcGAS #1 or #2) were treated with or without Talazoparib (10 µM for 72 hr). The cells were lysed and were immunoblotted using the indicated antibodies. Values were presented as means ± SD from three biological replicates. Significance was determined with two-way ANOVA. ****p < 0.0001, n.s., not significant. (**I**) RT-qPCR analyses of type I interferons. HeLa cells expressing shRNA against control (shScramble) or cGAS (shcGAS #1 or #2) were treated with or without Talazoparib (10 µM for 72 hr). Values of *Inf-α* and *Inf-β* mRNA levels were presented as means ± SEM from three biological replicates. Significance was determined with unpaired Student's t-test. ****p < 0.0001, n.s., not significant.

The online version of this article includes the following figure supplement(s) for figure 1:

Figure supplement 1. Proteomic profiling of PARPi-induced innate immune response (Part 1).
Figure supplement 2. Proteomic profiling of PARPi-induced innate immune response (Part 2).

(*Figure 1—figure supplement 1B*) or the subsequent DDR (*Figure 1—figure supplement 1C*). However, the activation of the innate immune response, as assessed by the level of pS172 TBK1 and the cGAS-STING target genes, was dramatically reduced in cGAS-depleted cells (*Figure 1H and I*, *Figure 1—figure supplement 1D*). Taken together, these results demonstrate that PARPi treatment induces the innate immune response via the cGAS-STING pathway.

To examine the immunomodulatory effects of PARPi in an unbiased manner, we performed isobaric labeling-based, global protein expression analysis in Talazoparib-treated MHH-ES-1 cells (an Ewing's sarcoma cell line that is highly sensitive to PARPi) (*Gill et al., 2015*). Talazoparib treatment was able to induce potent PARP1 trapping, γH2AX formation and TBK1 phosphorylation in this cell line (*Figure 1—figure supplement 2E–G*). Cells treated with DMSO or Talazoparib were lysed, and the proteins were digested with the resulting peptides labeled with the corresponding tandem mass tag (TMT) reagents. From this dataset, we were able to identify and quantify a total of 9545 proteins (protein false-discovery rate (FDR) < 1%) (*Supplementary file 1*). Correlation analysis revealed an excellent reproducibility between the biological replicate samples (*Figure 1—figure supplement 2H*). Compared to control, a total of 270 and 395 proteins were up- and down-regulated by at least two-fold, respectively, in Talazoparib-treated cells (*Figure 1—figure supplement 2I*). Intriguingly, gene ontology (GO) analyses of the up-regulated proteins showed that these proteins were highly enriched with biological processes connected to innate immune signaling (e.g., type I interferon signaling pathway, p=2.79 $\times$ 10^{-5} and immune response p=8.04 $\times$ 10^{-5}), which we validated using independent RT-qPCR assays (*Figure 1—figure supplement 2J and K*, *Supplementary file 2*). For example, we identified Interleukin 1α (IL1A) as one of the Talazoparib-induced, up-regulated cytokines in our quantitative proteomic dataset. Furthermore, Talazoparib treatment also induced the coordinated upregulation of several immune signaling proteins, including ISG15, IFIT3, MX1 and MX2 (*Supplementary file 1*).

PARP1 trapping is required for the PARPi-induced innate immune signaling

Because all FDA-approved PARPi possess both PARP1 trapping and PARP inhibition activities, we used a genetic method to assess their relative contribution to PARPi-induced activation of the cGAS-

STING pathway. Specifically, we generated PARP1 knock-out (KO) HeLa cells (**Figure 2—figure supplement 1A**) and found that Talazoparib treatment only induced PARP1 trapping in the wild-type (WT) cells, but not in PARP1 KO cells (**Figure 2A**). Accordingly, DDR, as detected by γH2AX, was also only elevated in the PARP1 WT cells (**Figure 2B**). Next, we evaluated whether the deletion of the PARP1 protein affects the PARPi-induced activation of the cGAS-STING pathway. As we expected, Talazoparib treatment led to a dramatic increase of pS172 TBK1 only in the PARP1 WT cells, but not PARP1 KO cells (**Figure 2C**). Talazoparib-induced IRF3 phosphorylation and its nuclear translocation were also blocked by PARP1 deletion (**Figure 2D**). Finally, PARP1 deletion also greatly diminished Talazoparib-induced expression of cGAS-STING target genes (**Figure 2E**, **Figure 2—figure supplement 1B**). These data indicate that the PARP1 protein is required for the PARPi-mediated activation of innate immune signaling.

We surveyed a series of clinically relevant PARPi, including Talazoparib, Niraparib, Rucaparib, Olaparib, and Veliparib. Consistent with previous studies, these compounds all potently blocked the enzymatic activity of PARP1 (**Figure 3—figure supplement 1A**). However, these compounds were able to induce different levels of PARP1 trapping (PARP1 trapping levels: Talazoparib > Niraparib > Rucaparib ≈ Olaparib > Veliparib) (**Figure 3A**). Interestingly, DDR as measured by γH2AX was correlative with respect to the level of PARP1 trapping elicited by these PARPi (DNA damage levels: Talazoparib > Niraparib > Rucaparib ≈ Olaparib > Veliparib) (**Figure 3B**). Accordingly, the cytotoxicity of these compounds also positively correlated with their PARP1 trapping activities (**Figure 3—figure supplement 1D**). Finally, the activation of the cGAS-STING pathway, as measured by the pS172 TBK level, also correlated with PARP1 trapping (**Figure 3C**). As an example, compared to Rucaparib, Talazoparib was able to induce a much stronger activation of the cGAS-STING pathway (**Figure 3—figure supplement 1B**). Taken together, these results showed that the level of PARP1 trapping, DNA damage, cytotoxicity and cGAS-STING activation was all positively correlated for the various PARPi (**Figure 3D**).

To further explore the role of PARP1 trapping in mediating the innate immune response of the PARPi, we employed a PARP1 mutant (R138C) that was identified from a chemical-induced mutagenesis screen performed in mouse embryonic stem cells (mESCs) (**Herzog et al., 2018**). This PARP1 mutant bears a significantly reduced DNA binding capability, and as a result, it cannot be trapped on the chromatin upon the treatment of PARPi. We generated PARP1 KO cells, and reconstituted these cells using either WT PARP1 or the PARP1 R138C mutant. Talazoparib treatment dramatically elevated the levels of PARP1 trapping in WT PARP1-reconsistuted cells, but not in cells reconstituted with the PARP1 R138C mutant (**Figure 3E**). Cells expressing the PARP1 R138C mutant also had greatly reduced DDR, upon Talazoparib treatment (**Figure 3F**). Finally, the expression of the PARP1 R138C mutant also prevented Talazoparib-induced activation of the cGAS-STING pathway (**Figure 3F and G**, **Figure 3—figure supplement 1C**). These results strongly supported the notion that PARP1 trapping is a prerequisite for the PARPi-induced activation of innate immune signaling.

PARP1 degraders block PARP1 without eliciting PARP1 trapping or the subsequent innate immune signaling

Using the Proteolysis Targeting Chimera (PROTAC) strategy, we recently developed a series of small molecule compounds that selectively degrade PARP1 (**Wang et al., 2019**). These compounds were derived by linking a PARPi (e.g., Rucaparib) and an E3 binder (e.g., pomalidomide) by a covalent chemical linker. Unlike regular PARPi, these compounds block both the enzymatic and scaffolding effects of PARP1, and thereby could dissect PARP1 inhibition vs. PARP1 trapping. Consistent with the notion that PARP1 trapping is a major contributor of the PARPi-induced cytotoxicity (**Wang et al., 2019**), the treatment of HeLa cells using one such compound (iRucaparib-AP6) led to robust downregulation of PARP1 in HeLa cells. In contrast, the parent compound (Rucaparib) only induced the cleavage, but not the degradation of PARP1, presumably because of its toxicity in these cells (**Figure 4A**). Using a different cell line system (i.e., MHH-ES-1), we also showed that Rucaparib, but not iRucaparib-AP6, strongly promoted cell death (**Figure 4—figure supplement 1**).

Consistent with the diminished pool of total PARP1, iRucaparib-AP6 treatment resulted in minimal PARP1 trapping and γH2AX formation (**Figure 4B and C**). Accordingly, the level of pS172 TBK1 were dramatically increased in Rucaparib-treated, but not in iRucaparib-AP6-treated cells (**Figure 4D**). We examined the expression of cGAS-STING target genes in these cells, and found
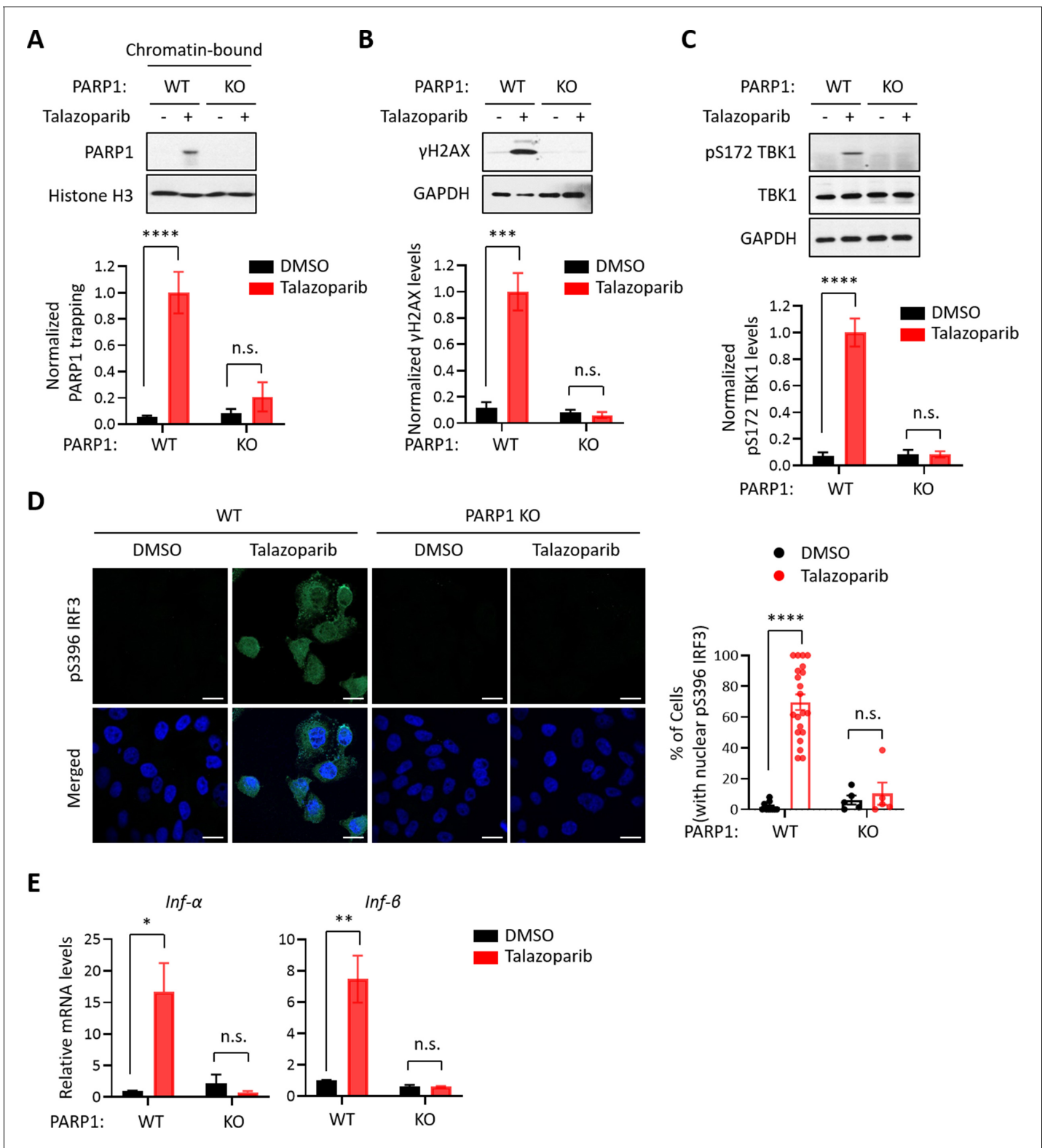
Figure 2. The PARP1 protein is required for PARPi-induced innate immune signaling. (**A**) PARPi-induced PARP1 trapping in wild-type (WT) and PARP1 knockout (KO) HeLa cells. Cell were also treated with or without Talazoparib (10 µM for 72 hr). Top, chromatin-bound fractions were isolated and were probed using the indicated antibodies. Histone H3 was used as the loading control. Bottom, the graph shows the quantification of the level of PARP1 trapping. Values were presented as means ± SD from three biological replicates. Significance was determined with two-way ANOVA. [****]p < 0.001, n.s., not significant. (**B**) DDR in WT and PARP1 KO HeLa cells treated with or without Talazoparib (10 µM for 72 hr). Top, whole cell lysates were probed

Figure 2 continued on next page

Figure 2 continued

using the indicated antibodies. Bottom, the graph shows the quantification of γH2AX levels. Values were presented as means ± SD from three biological replicates. Significance was determined with two-way ANOVA. ***p < 0.001, n.s., not significant. (C) The level of pS172 TBK1 in WT and PARP1 KO HeLa cells treated with or without Talazoparib (10 μM for 72 hr). Top, whole cell lysates were probed using the indicated antibodies. Bottom, the graph shows the quantification of pS172 TBK1 levels. Values were presented as means ± SD from three biological replicates. Significance was determined with two-way ANOVA. ****p < 0.0001, n.s., not significant. (D) Staining of pS396 IRF3 levels in WT and PARP1 KO HeLa cells treated with or without Talazoparib (10 μM for 72 hr). Left, a representative image of pS396 IRF3 levels (green). DAPI (blue) was used to visualize the nucleus. Right, the graph shows the quantification of the number of cells stained positive for pS396 IRF3 in the nucleus. Values were presented as means ± SEM from three biological replicates. Significance was determined with two-way ANOVA. ****p < 0.0001, n.s., not significant. (E) RT-qPCR analyses of type I interferons in WT and PARP1 KO HeLa cells treated with or without Talazoparib (10 μM for 72 hr). Values of *Inf-α* and *Inf-β* mRNA levels were presented as means ± SEM from three biological replicates. Significance was determined with two-way ANOVA. *p < 0.05, **p < 0.01, n.s., not significant.

The online version of this article includes the following figure supplement(s) for figure 2:

Figure supplement 1. The PARP1 protein is required for PARPi-induced innate immune response.

that Rucaparib, but not iRucaparib-AP6, treatment significantly elevated the mRNA levels of type I IFNs, pro-inflammatory cytokines and ISGs (*Figure 4E*).

Discussion

Since Rudolf Virchow observed the possible link between the immune system and tumors using lymphoid cells in a tumor in 1863, to use the immune system promoting antitumor response has been confirmed as one of the major breakthroughs in oncology, yielding the possibility of long-term clinical benefit and prolonged survival (*Zitvogel et al., 2008*; *Swann and Smyth, 2007*). The innate immune system as one of antitumor immune responses is composed of molecules and cells that respond to external and internal danger signals such as pathogen-associated molecular patterns (PAMPs) and damage-associated molecular patterns (DAMPs). PAMPs and DAMPs bind to their respective pattern recognition receptors (PRRs) to initiate immune responses. Thus, cytosolic PRRs including nucleotide-binding oligomerization domain–like receptors, retinoic acid–inducible gene I–like receptors (RLRs), and cGAS detect intracellular pathogens (*Wu and Chen, 2014*). Upon ligand binding, PRRs activate downstream signaling cascades to induce inflammatory responses such as the innate immune response, providing early protection against pathogen invasion or cellular damage.

Unlike normal cells, cancer cells are often replete with cytosolic dsDNA that originates from genomic, mitochondrial, and exogenous sources (*Vanpouille-Box et al., 2018*). Accumulating data have been reported that acute genomic stressors, including radiation, cisplatin, and intrinsic DNA damage generate cytosolic dsDNA and micronuclei to activate cGAS–STING in cancer cells (*Ahn et al., 2014*; *Harding et al., 2017*; *Mackenzie et al., 2017*; *Dou et al., 2017*). The role of PARPi as an inducer of DNA damage response has been well established to explain the cytotoxic effects of these compounds. However, accumulating evidence have pointed out that coordinated activation of both local and systemic antitumor immune responses could also underlie the antitumor effects of PARPi (*Pantelidou et al., 2019*; *Ding et al., 2018*; *Chabanon et al., 2019*).

Consistent with these previous studies, our date showed that PARPi treatment results in the robust production of cytosolic dsDNA, which leads to the subsequent activation of cGAS-STING signaling and the downstream innate immune pathway. The current PARPi are known to kill tumors via two distinct, but interconnected, mechanisms (i.e., PARP1 inhibition vs. PARP1 trapping) (*Zhen and Yu, 2018*; *Zhang et al., 2013*; *Wang et al., 2019*). The relative contribution of these two mechanisms in PARPi-mediated innate immune signaling, however, is poorly understood. Here, we sought to address this important question by using several independent systems. First, we found that the PARP1 protein is required for the PARPi-induced activation of cGAS-STING signaling. Indeed, Talazoparib was unable to cause PARP1 trapping, DDR and TBK1 activation in PARP1 KO cells. It is also important to note that the deletion of PARP1 alone does not lead to TBK1 activation and the expression of inflammatory genes, suggesting that the blockage of PARP1 catalytic activity is not sufficient to drive the activation of cGAS-STING signaling. Second, we found that the DNA-binding activity of PARP1 is required for the PARPi-induced activation of cGAS-STING signaling. Specifically, we employed a recently described PARP1 mutant (R138C) that was identified from an EMS-induced
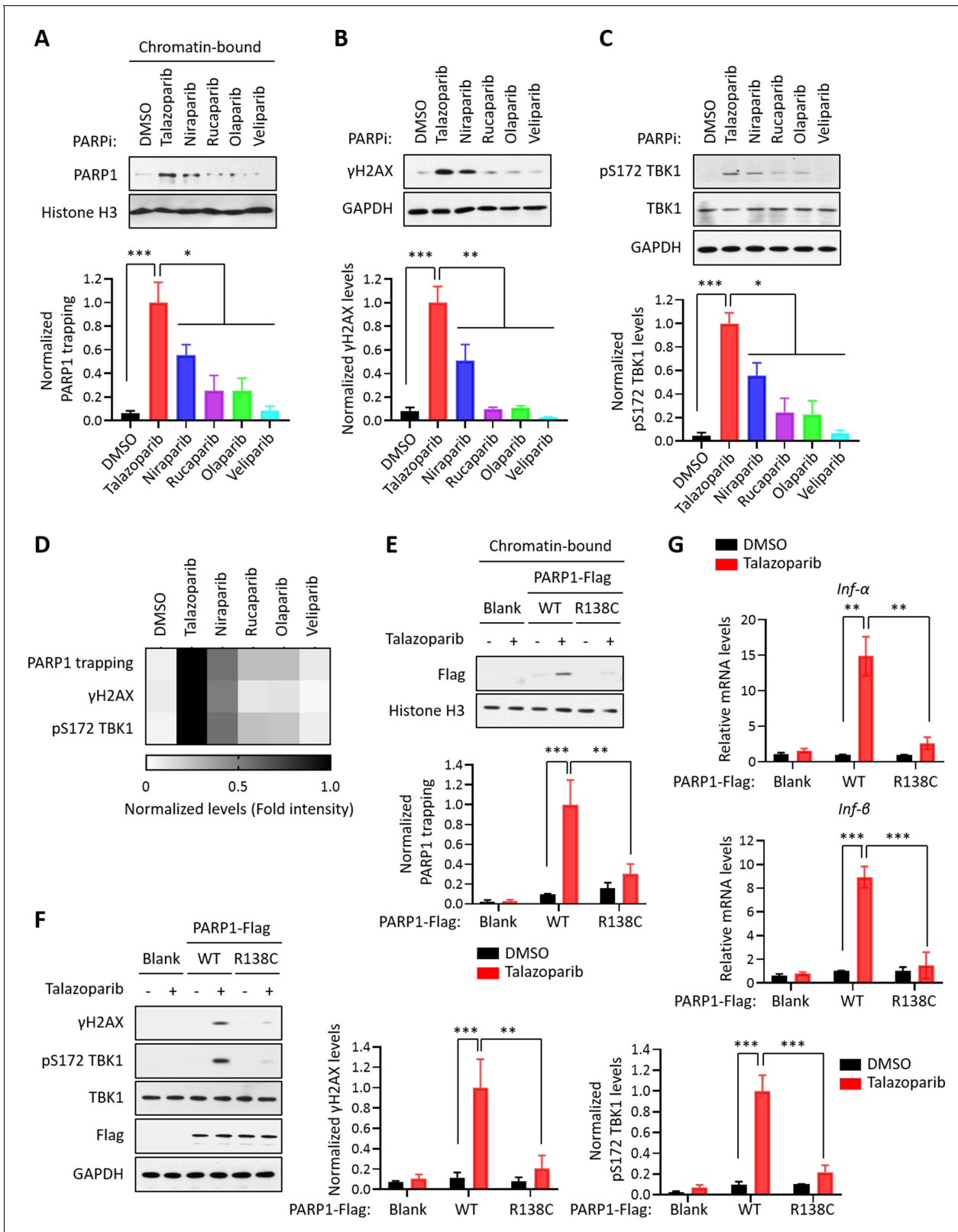
Figure 3. PARP1 trapping is the major contributor of PARPi-induced innate immune signaling. (**A**) The level of trapped PARP1 in HeLa cells treated with or without the indicated PARPi (10 μM for 72 hr). Top, chromatin-bound fractions were isolated and were probed using the indicated antibodies. Histone H3 was used as the loading control. Bottom, the graph shows the quantification of the level of PARP1 trapping. Values were presented as means ± SD from three biological replicates. Significance was determined with one-way ANOVA. *p < 0.05, ***p < 0.001. (**B**) The extent of DNA damage

Figure 3 continued on next page

Figure 3 continued

in HeLa cells treated with or without the indicated PARPi (10 µM for 72 hr). Top, whole cell lysates were probed using the indicated antibodies. Bottom, the graph shows the quantification of γH2AX levels. Values were presented as means ± SD from three biological replicates. Significance was determined with one-way ANOVA. $^{**}p < 0.01$, $^{***}p < 0.001$. (C) The level of pS172 TBK1 in HeLa cells treated with or without the indicated PARPi (10 µM for 72 hr). Top, whole cell lysates were probed using the indicated antibodies. Bottom, the graph shows the quantification of pS172 TBK1 levels. Values were presented as means ± SD from three biological replicates. Significance was determined with one-way ANOVA. $^{*}p < 0.05$, $^{***}p < 0.001$. (D) Heatmap of PARP1 trapping, DNA damage, and pS172 TBK1 levels for each PARPi. The normalized levels of PARP1 trapping (A), γH2AX (B), and pS172 TBK1 (C) are shown. (E) PARPi does not induce the trapping of a PARP1 mutant with defective DNA binding. Top, HeLa PARP1 KO cells expressing WT PARP1 or R138C mutant PARP1 (R138C) were treated with or without Talazoparib (10 µM for 72 hr). Chromatin-bound fractions were isolated and were probed using the indicated antibodies. Histone H3 was used as the loading control. Bottom, the graph shows the quantification of the levels of PARP1 trapping. Values were presented as means ± SD from three biological replicates. Significance was determined with two-way ANOVA. $^{**}p < 0.01$, $^{***}p < 0.001$. (F) The extent of DNA damage in HeLa PARP1 KO cells expressing WT PARP1 or R138C PARP1 that were treated with or without Talazoparib (10 µM for 72 hr). Left, whole cell lysates were probed using the indicated antibodies. Right, the graph shows the quantification of γH2AX and pS172 TBK1 levels. Values were presented as means ± SD from three biological replicates. Significance was determined with two-way ANOVA. $^{**}p < 0.01$, $^{***}p < 0.001$. (G) RT-qPCR analyses of type I interferons in HeLa PARP1 KO cells expressing WT or R138C PARP1 that were treated with or without Talazoparib (10 µM for 72 hr). Values of *Inf-α* and *Inf-β* mRNA levels were presented as means ± SEM from three biological replicates. Significance was determined with two-way ANOVA. $^{**}p < 0.01$, $^{***}p < 0.001$.

The online version of this article includes the following figure supplement(s) for figure 3:

Figure supplement 1. PARP1 trapping is required for PARPi-induced cytotoxicity and innate immune response.

random mutagenesis screen for resistance to a PARPi (i.e., Olaparib) (*Herzog et al., 2018*). This mutant is defective for DNA binding and PARP1 trapping, and mouse embryonic stem cells (mESCs) that bear this mutation are resistant to Olaparib. We generated PARP1-deleted cells and reconstituted them with either WT PARP1 or the PARP1 R138C mutant. We found that Talazoparib was able to induce DDR and cGAS-STING signaling only in cells expressing WT PARP1, but not the PARP1 R138C mutant. Third, we utilized a panel of 5 clinically relevant PARPi (i.e., Talazoaprib, Niraparib, Rucaparib, Olaparib, and Veliparib) (*Lord and Ashworth, 2017*). While these compounds all potently blocked the formation of PAR, they displayed a dramatically different capability in inducing PARP1 trapping. Indeed, a recent study showed that the different structural elements within these PARPi drive, in an allosteric manner, the release or retention of these compounds at a DNA break (*Zandarashvili et al., 2020*). Intriguingly, these compounds then induce DDR and activation of cGAS-STING signaling that is closely correlated with the degree of PARP1 trapping (*Figure 3A–D*, *Figure 3—figure supplement 1A and D*). Fourth, we utilized that a recently developed, 'non-trapping' PARP1 degrader (iRucaparib-AP6) (*Wang et al., 2019*). This compound is cell-membrane permeable and is able to block the enzymatic activity of PARP1. However, unlike regular PARPi, iRucaparib-AP6 degrades PARP1, which prevents PARP1 trapping, DDR, cytotoxicity, and finally, the activation of cGAS-STING signaling (*Figure 4*, *Figure 4—figure supplement 1*). Finally, recent studies have pointed to cytosolic dsDNA as a source of stimulus for the activation of cGAS-STING pathway (*Sun et al., 2013*; *Wu et al., 2014*; *Civril et al., 2013*). In the context of PAPRi, cytosolic dsDNA could result from PARPi-induced PARP1 trapping, and subsequently, stalled or collapsed replication forks. The detailed molecular underpinnings of this critical pathway need to be addressed in future studies.

In conclusion, we have identified a direct mechanism of the antitumor immune response of PARPi (*Figure 4F*). We demonstrated that the ability to induce PARP1 trapping is the primary driver for the PARPi-mediated cytotoxicity and activation of innate immune signaling in cancer cells. In the presence of PARP1, PARPi-induced PARP1 trapping generates cytosolic dsDNA, which activates cGAS, and the downstream innate immune response. Although the immunomodulatory roles of PARPi are highly desirable in human malignancies, the ability for PARP1 degraders to prevent PARP1 trapping, and hence the activation of innate immune response could be useful in other contexts (e.g., ischemia-reperfusion injury and neurodegenerative diseases). The full therapeutic potential of this class of compounds warrants further studies.
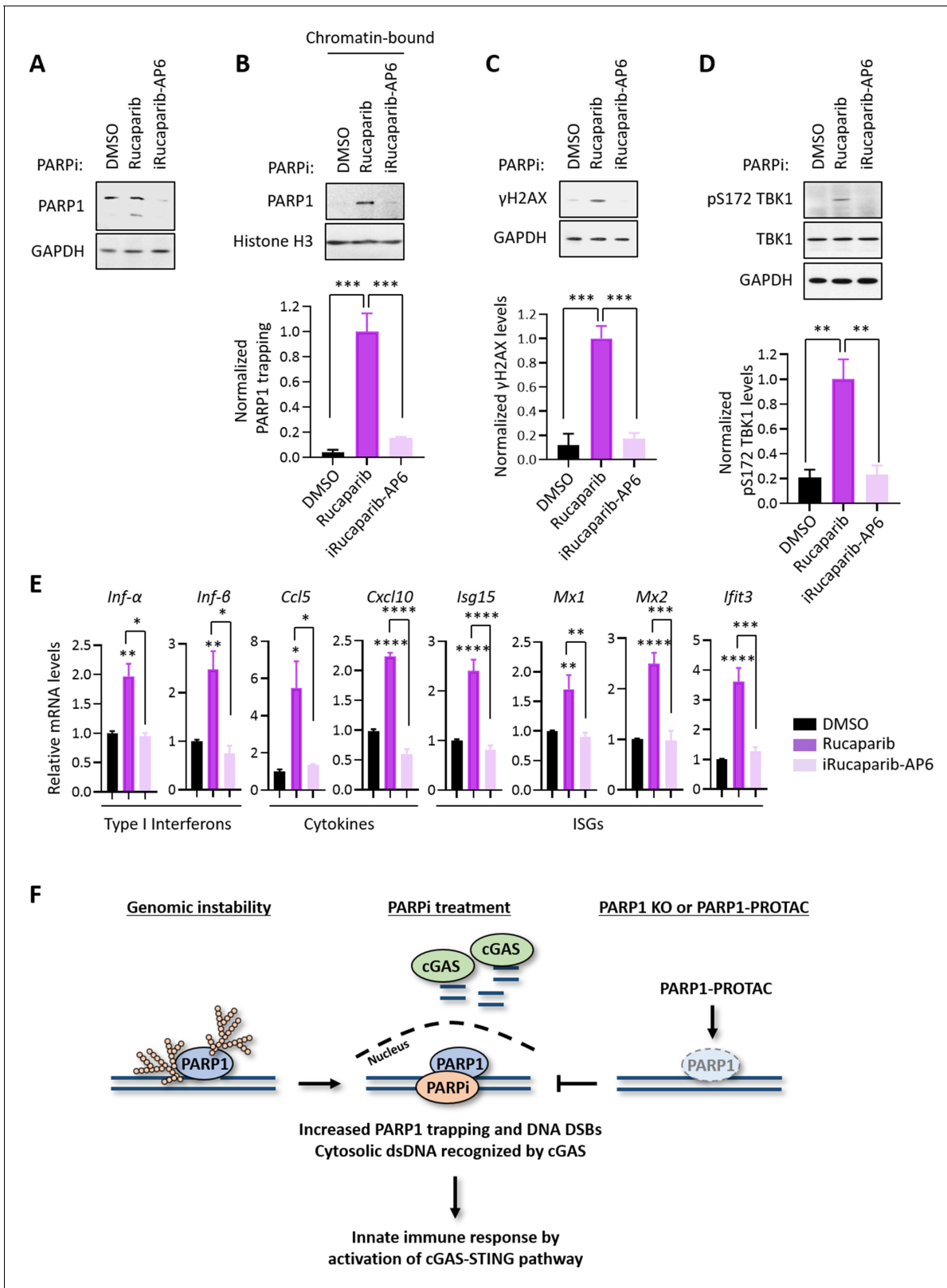
Figure 4. PARP1 degraders abolish PARP1-trapping induced innate immune signaling. (A) The level of PARP1 in HeLa cells treated with either Rucaparib or iRucaparib-AP6 (10 μM for 72 hr). Whole cell lysates were probed using the indicated antibodies. GAPDH was used as the loading control. (B) The level of trapped PARP1 in HeLa cells treated with either Rucaparib or iRucaparib-AP6 (10 μM for 72 hr). Top, chromatin-bound fractions were isolated and were probed using the indicated antibodies. Histone H3 was used as the loading control. Bottom, the graph shows the quantification of

Figure 4 continued on next page

Figure 4 continued

the level of PARP1 trapping. Values were presented as means ± SD from three biological replicates. Significance was determined with one-way ANOVA. ***p < 0.001. (**C**) The extent of DNA damage in HeLa cells treated with either Rucaparib or iRucaparib-AP6 (10 µM for 72 hr). Top, whole cell lysates were probed using the indicated antibodies. Bottom, the graph shows the quantification of γH2AX levels. Values were presented as means ± SD from three biological replicates. Significance was determined with one-way ANOVA. ***p < 0.001. (**D**) The level of pS172 TBK1 in HeLa cells treated with either Rucaparib or iRucaparib-AP6 (10 µM for 72 hr). Top, whole cell lysates were probed using the indicated antibodies. Bottom, the graph shows the quantification of pS172 TBK1 levels. Values were presented as means ± SD from three biological replicates. Significance was determined with one-way ANOVA. **p < 0.01. (**E**) RT-qPCR analyses of the cGAS-STING target gene expression in HeLa cells treated with either Rucaparib or iRucaparib-AP6 (10 µM for 72 hr). Values of type I interferons, cytokines, and ISGs mRNA levels were presented as means ± SEM from three biological replicates. Significance was determined with one-way ANOVA. *p < 0.05, **p < 0.01, ***p < 0.001, ****p < 0.0001. (**F**) The model of the activation of innate immune response via PARPi-induced PARP1 trapping.

The online version of this article includes the following figure supplement(s) for figure 4:

Figure supplement 1. PARP1 degraders prevent PARP1 trapping-induced cytotoxicity.

Materials and methods

Key resources table

Reagent type (species) or resource	Designation	Source or reference	Identifiers	Additional information
Antibody	Anti-PAR (Mouse monoclonal)	Trevigen	Cat# 4335-MC-100, RRID:AB_2572318	IB (1:3000)
Antibody	Anti-PARP1 (Rabbit polyclonal)	Cell Signaling Technology	Cat# 9542, RRID:AB_2160739	IB (1:1000)
Antibody	Anti-γH2AX (Rabbit monoclonal)	Cell Signaling Technology	Cat# 9718, RRID:AB_2118009	IB (1:3000)
Antibody	Anti-Histone H3 (Rabbit monoclonal)	Cell Signaling Technology	Cat# 4499, RRID:AB_10544537	IB (1:3000)
Antibody	Anti-GAPDH (Mouse monoclonal)	Santa Cruz Biotechnology	Cat# sc-32233, RRID:AB_627679	IB (1:5000)
Antibody	Anti-Phospho-TBK1/NAK (pS172 TBK1) (Rabbit monoclonal)	Cell Signaling Technology	Cat# 5483, RRID:AB_10693472	IB (1:1000)
Antibody	Anti-TBK1/NAK (Rabbit monoclonal)	Cell Signaling Technology	Cat# 3504, RRID:AB_2255663	IB (1:1000)
Antibody	Anti-Flag (Rabbit polyclonal)	MilliporeSigma	Cat# F7425, RRID:AB_439687	IB (1:1000)
Antibody	Anti-cGAS (Rabbit monoclonal)	Cell Signaling Technology	Cat# 15102, RRID:AB_2732795	IB (1:1000)
Antibody	Anti-Phospho-IRF-3 (pS396 IRF3) (Rabbit monoclonal)	Cell Signaling Technology	Cat# 4947, RRID:AB_823547	IF (1:1000)
Antibody	Alexa Fluor 488-conjugated goat anti-rabbit IgG (Goat polyclonal)	Thermo Fisher Scientific	Cat# A32731, RRID:AB_2633280	IF (1:1000)
Antibody	Goat Anti-Mouse IgG Antibody, HRP conjugate, Species Adsorbed (Goat polyclonal)	MilliporeSigma	Cat# AP181P, RRID:AB_11214094	IB (1:3000)
Antibody	ECL Rabbit IgG, HRP-linked fragment (Donkey polyclonal)	GE Healthcare life sciences	Cat# NA9340, RRID:AB_772191	IB (1:3000)

Continued on next page

Continued

Reagent type (species) or resource	Designation	Source or reference	Identifiers	Additional information
Chemical compound, drug	Talazoparib	Selleck	Cat# S7048	PARP1 inhibitor
Chemical compound, drug	Niraparib	Selleck	Cat# S2741	PARP1 inhibitor
Chemical compound, drug	Rucaparib	Selleck	Cat# S1098	PARP1 inhibitor
Chemical compound, drug	Olaparib	Selleck	Cat# S1060	PARP1 inhibitor
Chemical compound, drug	Veliparib	Selleck	Cat# S1004	PARP1 inhibitor
Chemical compound, drug	iRucaparib-AP6	Our laboratory	N/A	PARP1 degrader
Chemical compound, drug	Polybrene (Hexadimethrine bromide)	MilliporeSigma	Cat# H9268; CAS 28728-55-4	
Chemical compound, drug	Puromycin	MilliporeSigma	Cat# P7255; CAS 58-58-2	
Cell line (human)	HeLa	ATCC	Cat# CCL-2, RRID:CVCL_0030	
Cell line (human)	HeLa PARP1 KO	In this study	N/A	PARP1 deficient HeLa
Cell line (human)	MHH-ES-1	DSMZ	Cat# ACC 167, RRID:CVCL_1411	
Cell line (human)	HeLa	ATCC	Cat# CCL-2	
Recombinant DNA reagent	pCMV-hPARP1-3xFlag-WT	Addgene	Cat# 11157	In pCMV; tagged with 3XFlag on its N-terminus
Recombinant DNA reagent	pCMV-hPARP1-3xFlag-R138C	In this study	Modified by R138C mutation	In pCMV; tagged with 3XFlag on its N-terminus
Strain, strain background (*Escherichia coli*)	DH5alpha	Thermo Fisher Scientific	Cat# 18258012	Competent cells
Strain, strain background (*Escherichia coli*)	Stbl3 Competent *E. coli*	Thermo Fisher Scientific	Cat# C737303	Competent cells
Commercial assay or kit	Quant-iT PicoGreen dsDNA Reagent	Thermo Fisher Scientific	Cat# P7581	
Commercial assay or kit	Subcellular Protein Fractionation Kit for Cultured Cells	Thermo Fisher Scientific	Cat# 78840	
Commercial assay or kit	RNeasy Mini Kit	QIAGEN	Cat# 74104	
Commercial assay or kit	QIAprep Spin Miniprep Kit	QIAGEN	Cat# 27106	
Commercial assay or kit	e-Myco PLUS Mycoplasma PCR Detection Kit	BOCA SCIENTIFIC	Cat# 25237	
Commercial assay or kit	TMT6plex Mass Tag Labeling Kits	Thermo Fisher Scientific	Cat# 90110	
Commercial assay or kit	CellTiter-Glo Luminescent Cell Viability Assay	Promega	Cat# G7571	
Software, algorithm	ImageJ 1.49 v	NIH	https://imagej.net/ImageJ2	
Software, algorithm	DAVID Bioinformatics Resources v6.8	DAVID	https://david.ncifcrf.gov/	
Software, algorithm	PRISM v8.2.0	GraphPad	https://www.graphpad.com/scientific-software/prism/	

Continued on next page

Continued

Reagent type (species) or resource	Designation	Source or reference	Identifiers	Additional information
Software, algorithm	human protein sequences (Uniprot)	UniProt	https://www.uniprot.org/UniProt database (2019_07,560,537 sequences;taxonomy, *Homo sapiens*, 20,431)	
Software, algorithm	human IPI protein database v3.60	EMBL-EBI	ftp://ftp.ebi.ac.uk/pub/databases/IPI	
Software, algorithm	The Sequest algorithm v28	Cell. 2010 Dec 3 ;143(7):1174–89	N/A	
Others	DAPI	MilliporeSigma	Cat# D9542	
Others	Dimethyl sulfoxide (DMSO)	Thermo Fisher Scientific	Cat# BP231-1; CAS 67-68-5	
Others	Lipofectamine 2000	Thermo Fisher Scientific	Cat# 11668500	
Others	Dulbecco's Modified Eagle's Medium (DMEM)	MilliporeSigma	Cat# D5796	
Others	RPMI1640	MilliporeSigma	Cat# R8758	
Others	Fetal Bovine Serum (FBS)	MilliporeSigma	Cat# 12303C	
Others	Lysyl Endopeptidase (Lys-C)	Wako	Cat# 129–02541; CAS 123175-82-6	
Others	Gen5	BioTek	N/A	
Others	BCA reagents	Thermo Fisher Scientific	Cat# 23224/23228	
Others	0.45 μm filter	Thermo Fisher Scientific	Cat# 05-713-387	
Others	Synergy HT Multi-Detection Microplate Reader.	BioTek	N/A	
Others	SuperScript III Reverse Transcriptase	Thermo Fisher Scientific	Cat# 18080044	
Others	CFX384 Touch Real-Time PCR Detection System	Bio-Rad	Cat# 1855484	
Others	Applied Biosystems Power SYBR Green PCR Master Mix	Thermo Fisher Scientific	Cat# 43-676-59	
Others	Oasis HLB solid-phase extraction (SPE) cartridges	Waters	Cat# 186000383	
Others	3M Empore C18 Extraction Disk	Thermo Fisher Scientific	Cat# 14-386-2	
Others	ZORBAX 300Extend-C18 HPLC column	Agilent	Cat# 761775–902	
Others	Q Exactive Hybrid Quadrupole-Orbitrap Mass Spectrometer	Thermo Fisher Scientific	Cat# IQLAAEGAAPFALGMAZR	
Others	PicoFrit nanospray columns	New Objective	PF360-75-15-N-5	

Cell lines and culture procedures

Human cervical carcinoma cells (HeLa, from ATCC) were maintained in high glucose Dulbecco's Modified Eagle's Medium (DMEM) (MilliporeSigma), supplemented with 10% Fetal bovine serum (FBS) (MilliporeSigma) at 37℃ in 5% CO_2. Human Ewing's Sarcoma cells (MHH-ES-1, from DSMZ) were maintained in RPMI1640 (MilliporeSigma), supplemented with 10% Fetal bovine serum (FBS) (MilliporeSigma) at 37℃ in 5% CO_2. All cell lines have been DNA fingerprinted using the PowerPlex 1.2 kit (Promega) and are found to be mycoplasma free using the e-Myco kit (Boca Scientific). The concentrations and times of each chemical treatment are indicated in the figure legends.

Antibodies and reagents

Antibodies against the following proteins were used. Cell Signaling Technology: PARP1 (#9542), γH2AX (#9718), Histone H3 (#4499), Phospho-TBK1/NAK (pS172 TBK1; #5483), TBK1/NAK (#3504), cGAS (#15102), STING (#13647), Phospho-IRF-3 (pS396 IRF3; #4947); Santa Cruz Biotechnology: GAPDH (#sc-32233); Trevigen: PAR (#4335-MC-100); MilliporeSigma: Flag (#F7425). Thermo Fisher: Alexa Fluor 488-conjugated goat anti-rabbit IgG (Cat# A32731). The following reagents were used: Talazoparib, Niraparib, Rucaparib, Olaparib, and Veliparib were all purchased from Selleck; iRuca-parib-AP6 was synthesized in previous our report (Wang et al., 2019). Dimethyl sulfoxide (DMSO), and Lipofectamine 2000 were all purchased from Thermo Fisher Scientific; Polybrene (Hexadimethrine bromide) and Puromycin were purchased from MilliporeSigma.

Immunoblot analysis

Cellular lysates were prepared using a 1% SDS lysis buffer containing 10 mM HEPES, pH 7.0, 2 mM $MgCl_2$, 20 U/mL universal nuclease. Cellular lysates were clarified by centrifugation at 14,000 × g at 4°C for 15 min. Protein concentrations were determined with the BCA assay (Thermo Fisher Scientific). The resulting supernatants were subjected to immunoblot analysis with the corresponding antibodies. Enhanced chemiluminescence was used to detect specific bands using standard methods as previously described (Kim et al., 2016). The relative band intensity was measured using the Image J imaging software.

Immunofluorescence

For immunofluorescence localization of the target molecules, HeLa PARP1 WT and KO cells were cultured on the cover glasses. Cells were fixed with 4% paraformaldehyde (Electron Microscopy Sciences, Hatfield, PA, USA) and blocked for 1 hr at RT in PBS (Lonza, Basel, Switzerland) containing 5% FBS and 0.2% Triton X-100. Cells were then incubated with a Rabbit monoclonal anti-pS396 IRF3 antibody overnight at 4°C, followed by incubation with an Alexa Fluor 488-conjugated goat anti-rabbit IgG (Thermo Fisher). For PicoGreen staining, cells were incubated with the Quant-iT PicoGreen dsDNA reagent (Thermo Fisher) overnight at 4°C. Fluorescence images were observed under an LSM 510 META confocal laser scanning microscope equipped with epifluorescence and an LSM digital image analyzer (Carl Zeiss, Zana, Germany). DAPI (Molecular Probes, Eugene, OR, USA) was used as a counter staining probe to mark the nuclei.

Cellular fractionation

Cells were biochemically fractionated using a subcellular protein fractionation kit (Thermo Fisher Scientific, USA) according to the manufacturer's instructions. Briefly, cells were harvested with trypsin-EDTA, centrifuged at 500 × g for 5 min and washed with ice-cold PBS. After adding the CEB buffer to the cell pellet, the tube was incubated at 4°C for 10 min with gentle mixing. Following centrifugation at 500 × g for 5 min, the supernatant (the cytoplasmic extract) was transferred to a clean pre-chilled tube on ice. Next, the MEB buffer was added to the pellet. The tube was briefly vortexed and was incubated at 4°C for 10 min with gentle mixing. The tube was then centrifuged at 3000 × g for 5 min and the supernatant (the membrane extract) was transferred to a clean pre-chilled tube on ice. An ice-cold NEB buffer was added to the pellet, and the tube was vortexed using the highest setting for 15 s. Following incubation at 4°C for 30 min with gentle mixing, the tube was centrifuged at 5000 × g for 5 min and the supernatant (the soluble nuclear extract) was transferred to a clean pre-chilled tube on ice. Lastly, the room temperature NEB buffer containing Micrococcal Nuclease and $CaCl_2$ was added to the pellet. The tube was vortexed for 15 s and incubated at room temperature for 15 min. After incubation, the tube was centrifuged at 16,000 × g for 5 min and the supernatant (the chromatin-bound nuclear extract) was transferred to a clean pre-chilled tube on ice.

Plasmids and mutagenesis

Flag-tagged PAPR1 WT (PARP1-Flag; #111575) was purchased from Addgene. The Flag-tagged PARP1 R138C mutant was generated by the site-directed mutagenesis Kit (Agilent, La Jolla, CA, USA) according to the manufacturer's instructions. The plasmids were subjected to DNA sequencing for verification.

CRISPR/Cas9-mediated PARP1 knockout (KO)

In order to knock out PARP1 via the CRISPR/Cas9 system, sgRNAs of PARP1 were designed using the CRISPR design website (http://crispr.mit.edu/) and were incorporated into the lentiCRISPR_v2 plasmid. Cells were then plated in 6-well plates and were transfected with these plasmids. After 24 hr of culture and puromycin selection (1 μg/ml), single cells were sorted into 96-well plates. After a 2 week culture period, protein lysates were extracted and PARP1 KO was confirmed by immunoblot analysis. The sgRNAs were listed (See also *Supplementary file 3*).

Cell viability measurement

MHH-ES-1 cells were plated into 96-well plates at densities of 1000 cells/well. One day later, cells were treated with various PARP inhibitors and iRucaparib-AP6 as indicated. Cell viability was measured using the CellTiter-Glo assay (Promega) according to the manufacturer's instructions. Briefly, after incubation, room temperature CellTiter-Glo reagent was added 1:1 to each well and the plates were incubated at room temperature for 2 min. Luminescence was measured with the Synergy HT Multi-Detection Microplate Reader and was normalized against control cells treated with DMSO.

RNA interference and transfection

To produce the lentiviruses, shRNA plasmids were co-transfected into HEK293TD cells along with packaging (Δ8.9) and envelope (VSVG) expression plasmids using the Lipofectamine 2000 reagent (Invitrogen) according to the manufacturer's instructions. The next day, the media was refreshed. After two days, viral supernatants were collected and filtered using a 0.45 μm filter. Recipient cells were infected in the presence of a serum-containing medium supplemented with 8 μg/ml Polybrene. Two days after infection, cells were used for the indicated experiments. Lipofectamine 2000 reagents were also used to transiently knock-down or over-express the target genes, according to the manufacturer's instructions. Two days after infection or transfection, the cells were used for the indicated experiments. The knock-down or over-expression of target genes was validated by immunoblot assays. The following shRNA constructs and over-expression plasmids were used (See also *Supplementary file 3*). The cGAS knockdown for RNA interference was achieved using Mission shRNA-encoding lentivirus directed to human cGAS mRNA (Sigma; GenBank/EMBL/DDBJ accession no. NM_138441) as recommended by the manufacturer's protocols. Briefly, lentiviral vectors (in pLKO.1) containing cGAS shRNA sequences (shcGAS #1, TRCN0000428336; shcGAS #2, TRCN0000149811) and non-target shRNA control vector (shScramble, SHC016) were purchased from Sigma.

Real-time quantitative polymerase chain reaction (RT-qPCR)

The mRNA extraction was performed using the RNeasy Mini Kit (QIAGEN) according to the manufacturer's instructions. Subsequently, total RNAs were converted into cDNA using the SuperScript III Reverse Transcriptase (Thermo Fisher Scientific) following the manual for first-strand cDNA synthesis. qPCR reactions were performed on a CFX384 Touch Real-Time PCR Detection System using 2X Power SYBR Green PCR Master Mix (Thermo Fisher Scientific). For each condition, technical triplicates were prepared and the quantitation cycle (Cq) was calculated. For normalization, GAPDH levels were used as an internal reference and the relative expression levels were presented. The primers used in qPCR were listed (See also *Supplementary file 3*).

Sample preparation for mass spectrometry

MHH-ES-1 cells were treated with or without Talazoparib (0.1 or 1 μM) for 24 hr. Cells were lysed with 1% SDS lysis buffer containing 10 mM HEPES, pH 7.0, 2 mM MgCl$_2$, 20 U/mL universal nuclease. Protein concentrations were determined with the BCA assay (Thermo Fisher Scientific). Samples from two biological replicates were reduced with 3 mM dithiothreitol (DTT) for 20 min and were alkylated with 25 mM iodoacetamide (IDA) for 30 min at room temperature (RT) in dark. The detergents were removed by methanol/chloroform precipitation. The proteins were re-solubilized in 8 M urea and digested by Lys-C at a 1:100 (w/w) enzyme/protein ratio for 2 hr, followed by trypsin digestion at a 1:100 (w/w) enzyme/protein ratio overnight at RT in 2 M urea. The peptides were desalted using Oasis HLB solid-phase extraction (SPE) cartridges (Waters) (*Erickson et al., 2015*) and approximately 100 μg of peptides from each sample were re-suspended in 200 mM HEPES, pH 8.5. The

peptides were then labeled with the amine-based TMT 6-plex reagents (Thermo Fisher) for 1 hr at RT. Hydroxylamine solution was added to quench the reaction and the labeled peptide samples were combined. The TMT samples were lyophilized and reconstituted in buffer A (10 mM Ammonium formate, pH 10.0). Samples were centrifuged at 10,000 $\times$ g for 3 min using spin-X centrifuge tube filters (Thermo Fisher Scientific) prior to loading onto a ZORBAX 300Extend-C18 HPLC column (Agilent, Narrow Bore RR 2.1 mm x 100 mm, 3.5 µm particle size, 300 Å pore size). Peptides were fractionated by bRPLC (basic pH reversed phase HPLC) at a 0.2 mL/min flow rate using a gradient from 0% to 70% buffer B (1% Ammonium formate, pH 10.0% and 90% Acetonitrile). A total of seventeen fractions were collected, which were lyophilized, desalted, and analyzed by LC-MS/MS experiments.

Quantitative proteomic analysis by LC-MS/MS

The TMT samples were analyzed on a Q-Exactive HF Mass Spectrometer (Thermo Fisher Scientific). MS/MS spectra were searched against a composite database of human protein sequences (Uniprot) and their reversed complement using the Sequest algorithm (Ver28) embedded in an in-house-developed software suite (*Huttlin et al., 2010*). MS1 and MS2 mass tolerances were set to be 50 ppm and 0.05 Da, respectively. Search parameters allowed for full tryptic peptides (two missed cleavage sites) with a static modification of 57.02146 Da on cystine (Carbamidomethyl), a variable modification of 15.994915 Da on methionine (oxidation), and a static modification of TMT labels (229.16293 Da) on peptide N-terminus and lysine. Search results were filtered to include <1% matches (both peptide and protein level filtering) to the reverse database by the linear discriminator function using parameters including Xcorr, dCN, missed cleavage, charge state (exclude 1+ peptides), mass accuracy, peptide length, and fraction of ions matched to MS/MS spectra. Peptide quantification was performed by using the CoreQuant algorithm implemented in an in-house-developed software suite (*Erickson et al., 2017*). The labeling scheme for the TMT experiments is: 126: DMSO; 127: Talazoparib (0.1 µM); 128: Talazoparib (1 µM), 129: Talazoparib (1 µM); 130: Talazoparib (0.1 µM); 131: DMSO. For TMT quantification, a 0.03 Th window was scanned around the theoretical m/z of each reporter ion (126: 126.127726; 127: 127.124761; 128: 128.134436; 129: 129.131471; 130: 130.141145; 131: 131.138180) to detect the presence of these ions. The maximum intensity of each ion was extracted, and the signal-to-noise (SN) value of each protein is calculated by summing the reporter ion counts across all identified peptides. Because the same amount of peptides was used for each TMT channel, the total reporter ion intensity of each channel was summed across all quantified proteins, and was then normalized and reported. Data were exported to Excel for further analysis.

Statistics

All statistical analyses including unpaired Student's t-tests, one- and two-way ANOVA tests were performed using the GraphPad Prism software (v8.2.0). The type of statistical analyses, parameters, and number of replicates are indicated for each experiment in the figure legends. Data were calculated as mean ± SEM or SD. The following indications of significance were used throughout the manuscript: *p < 0.05, **p < 0.01, ***p < 0.001, ****p < 0.0001, n.s, not significant.

Additional information

Competing interests

Yonghao Yu: A patent application on the PARP degraders was previously filed (PCT/US2020/016129). The other authors declare that no competing interests exist.

Author ORCIDs

Chiho Kim (ID) https://orcid.org/0000-0001-6846-5515
Xu-Dong Wang (ID) http://orcid.org/0000-0002-8265-1485
Yonghao Yu (ID) https://orcid.org/0000-0001-8414-4666

Decision letter and Author response

Decision letter https://doi.org/10.7554/eLife.60637.sa1
Author response https://doi.org/10.7554/eLife.60637.sa2

Additional files

Supplementary files

• Supplementary file 1. Raw and analyzed TMT-MS data in MHH-ES-1 following Talazoparib treatment (1 µM for 24 hr).

• Supplementary file 2. GO analysis of up-regulated proteins from *Supplementary file 1*.

• Supplementary file 3. Oligo sequence in this study.

• Transparent reporting form

Data availability

The raw and analyzed TMT-MS data in MHH-ES-1 cells following Talazoparib treatment is provided in Supplementary file 1. Its GO analysis data using up-regulated proteins is provided in Supplementary file 2.

References

Ahn J, Xia T, Konno H, Konno K, Ruiz P, Barber GN. 2014. Inflammation-driven carcinogenesis is mediated through STING. *Nature Communications* **5**:5166. DOI: https://doi.org/10.1038/ncomms6166, PMID: 25300616

Barber GN. 2015. STING: infection, inflammation and Cancer. *Nature Reviews Immunology* **15**:760–770. DOI: https://doi.org/10.1038/nri3921, PMID: 26603901

Chabanon RM, Muirhead G, Krastev DB, Adam J, Morel D, Garrido M, Lamb A, Hénon C, Dorvault N, Rouanne M, Marlow R, Bajrami I, Cardeñosa ML, Konde A, Besse B, Ashworth A, Pettitt SJ, Haider S, Marabelle A, Tutt AN, et al. 2019. PARP inhibition enhances tumor cell-intrinsic immunity in ERCC1-deficient non-small cell lung Cancer. *Journal of Clinical Investigation* **129**:1211–1228. DOI: https://doi.org/10.1172/JCI123319, PMID: 305 89644

Chen Q, Sun L, Chen ZJ. 2016. Regulation and function of the cGAS-STING pathway of cytosolic DNA sensing. *Nature Immunology* **17**:1142–1149. DOI: https://doi.org/10.1038/ni.3558, PMID: 27648547

Civril F, Deimling T, de Oliveira Mann CC, Ablasser A, Moldt M, Witte G, Hornung V, Hopfner KP. 2013. Structural mechanism of cytosolic DNA sensing by cGAS. *Nature* **498**:332–337. DOI: https://doi.org/10.1038/nature12305, PMID: 23722159

Ding L, Kim HJ, Wang Q, Kearns M, Jiang T, Ohlson CE, Li BB, Xie S, Liu JF, Stover EH, Howitt BE, Bronson RT, Lazo S, Roberts TM, Freeman GJ, Konstantinopoulos PA, Matulonis UA, Zhao JJ. 2018. PARP inhibition elicits STING-Dependent antitumor immunity in Brca1-Deficient ovarian Cancer. *Cell Reports* **25**:2972–2980. DOI: https://doi.org/10.1016/j.celrep.2018.11.054, PMID: 30540933

Dou Z, Ghosh K, Vizioli MG, Zhu J, Sen P, Wangensteen KJ, Simithy J, Lan Y, Lin Y, Zhou Z, Capell BC, Xu C, Xu M, Kieckhaefer JE, Jiang T, Shoshkes-Carmel M, Tanim K, Barber GN, Seykora JT, Millar SE, et al. 2017. Cytoplasmic chromatin triggers inflammation in senescence and Cancer. *Nature* **550**:402–406. DOI: https://doi.org/10.1038/nature24050, PMID: 28976970

Erickson BK, Jedrychowski MP, McAlister GC, Everley RA, Kunz R, Gygi SP. 2015. Evaluating multiplexed quantitative phosphopeptide analysis on a hybrid quadrupole mass filter/linear ion trap/orbitrap mass spectrometer. *Analytical Chemistry* **87**:1241–1249. DOI: https://doi.org/10.1021/ac503934f, PMID: 25521595

Erickson BK, Rose CM, Braun CR, Erickson AR, Knott J, McAlister GC, Wühr M, Paulo JA, Everley RA, Gygi SP. 2017. A strategy to combine sample multiplexing with targeted proteomics assays for High-Throughput protein signature characterization. *Molecular Cell* **65**:361–370. DOI: https://doi.org/10.1016/j.molcel.2016.12.005, PMID: 28065596

Faraoni I, Graziani G. 2018. Role of BRCA mutations in Cancer treatment with Poly(ADP-ribose) Polymerase (PARP) Inhibitors. *Cancers* **10**:487. DOI: https://doi.org/10.3390/cancers10120487

Farmer H, McCabe N, Lord CJ, Tutt AN, Johnson DA, Richardson TB, Santarosa M, Dillon KJ, Hickson I, Knights C, Martin NM, Jackson SP, Smith GC, Ashworth A. 2005. Targeting the DNA repair defect in BRCA mutant cells as a therapeutic strategy. *Nature* **434**:917–921. DOI: https://doi.org/10.1038/nature03445, PMID: 1582 9967

Fu Y, Fang Y, Lin Z, Yang L, Zheng L, Hu H, Yu T, Huang B, Chen S, Wang H, Xu S, Bao W, Chen Q, Sun L. 2020. Inhibition of cGAS-Mediated interferon response facilitates transgene expression. *iScience* **23**:101026. DOI: https://doi.org/10.1016/j.isci.2020.101026, PMID: 32283527

Gibson BA, Kraus WL. 2012. New insights into the molecular and cellular functions of poly(ADP-ribose) and PARPs. *Nature Reviews Molecular Cell Biology* **13**:411–424. DOI: https://doi.org/10.1038/nrm3376, PMID: 22713970

Gill SJ, Travers J, Pshenichnaya I, Kogera FA, Barthorpe S, Mironenko T, Richardson L, Benes CH, Stratton MR, McDermott U, Jackson SP, Garnett MJ. 2015. Combinations of PARP inhibitors with temozolomide drive PARP1 trapping and apoptosis in Ewing's Sarcoma. *PLOS ONE* **10**:e0140988. DOI: https://doi.org/10.1371/journal.pone.0140988, PMID: 26505995

Glück S, Guey B, Gulen MF, Wolter K, Kang TW, Schmacke NA, Bridgeman A, Rehwinkel J, Zender L, Ablasser A. 2017. Innate immune sensing of cytosolic chromatin fragments through cGAS promotes senescence. *Nature Cell Biology* **19**:1061–1070. DOI: https://doi.org/10.1038/ncb3586, PMID: 28759028

Harding SM, Benci JL, Irianto J, Discher DE, Minn AJ, Greenberg RA. 2017. Mitotic progression following DNA damage enables pattern recognition within micronuclei. *Nature* **548**:466–470. DOI: https://doi.org/10.1038/nature23470, PMID: 28759889

Herzog M, Puddu F, Coates J, Geisler N, Forment JV, Jackson SP. 2018. Detection of functional protein domains by unbiased genome-wide forward genetic screening. *Scientific Reports* **8**:6161. DOI: https://doi.org/10.1038/s41598-018-24400-4, PMID: 29670134

Hopkins TA, Ainsworth WB, Ellis PA, Donawho CK, DiGiammarino EL, Panchal SC, Abraham VC, Algire MA, Shi Y, Olson AM, Johnson EF, Wilsbacher JL, Maag D. 2019. PARP1 trapping by PARP inhibitors drives cytotoxicity in both Cancer cells and healthy bone marrow. *Molecular Cancer Research* **17**:409–419. DOI: https://doi.org/10.1158/1541-7786.MCR-18-0138, PMID: 30429212

Huttlin EL, Jedrychowski MP, Elias JE, Goswami T, Rad R, Beausoleil SA, Villén J, Haas W, Sowa ME, Gygi SP. 2010. A tissue-specific atlas of mouse protein phosphorylation and expression. *Cell* **143**:1174–1189. DOI: https://doi.org/10.1016/j.cell.2010.12.001, PMID: 21183079

Ishikawa H, Barber GN. 2008. STING is an endoplasmic reticulum adaptor that facilitates innate immune signalling. *Nature* **455**:674–678. DOI: https://doi.org/10.1038/nature07317, PMID: 18724357

Kato K, Omura H, Ishitani R, Nureki O. 2017. Cyclic GMP–AMP as an Endogenous Second Messenger in Innate Immune Signaling by Cytosolic DNA. *Annual Review of Biochemistry* **86**:541–566. DOI: https://doi.org/10.1146/annurev-biochem-061516-044813

Kim C, Yun N, Lee J, Youdim MB, Ju C, Kim WK, Han PL, Oh YJ. 2016. Phosphorylation of CHIP at Ser20 by Cdk5 promotes tAIF-mediated neuronal death. *Cell Death & Differentiation* **23**:333–346. DOI: https://doi.org/10.1038/cdd.2015.103, PMID: 26206088

Li T, Chen ZJ. 2018. The cGAS-cGAMP-STING pathway connects DNA damage to inflammation, senescence, and Cancer. *Journal of Experimental Medicine* **215**:1287–1299. DOI: https://doi.org/10.1084/jem.20180139, PMID: 29622565

Liang Y, Peng H. 2016. STING-cytosolic DNA sensing: the backbone for an effective tumor radiation therapy. *Annals of Translational Medicine* **4**:60. DOI: https://doi.org/10.3978/j.issn.2305-5839.2015.12.48, PMID: 269045 82

Lord CJ, Tutt AN, Ashworth A. 2015. Synthetic lethality and Cancer therapy: lessons learned from the development of PARP inhibitors. *Annual Review of Medicine* **66**:455–470. DOI: https://doi.org/10.1146/annurev-med-050913-022545, PMID: 25341009

Lord CJ, Ashworth A. 2017. PARP inhibitors: synthetic lethality in the clinic. *Science* **355**:1152–1158. DOI: https://doi.org/10.1126/science.aam7344, PMID: 28302823

Mackenzie KJ, Carroll P, Martin CA, Murina O, Fluteau A, Simpson DJ, Olova N, Sutcliffe H, Rainger JK, Leitch A, Osborn RT, Wheeler AP, Nowotny M, Gilbert N, Chandra T, Reijns MAM, Jackson AP. 2017. cGAS surveillance of micronuclei links genome instability to innate immunity. *Nature* **548**:461–465. DOI: https://doi.org/10.1038/nature23449, PMID: 28738408

Motwani M, Pesiridis S, Fitzgerald KA. 2019. DNA sensing by the cGAS-STING pathway in health and disease. *Nature Reviews Genetics* **20**:657–674. DOI: https://doi.org/10.1038/s41576-019-0151-1, PMID: 31358977

Murai J, Huang SY, Das BB, Renaud A, Zhang Y, Doroshow JH, Ji J, Takeda S, Pommier Y. 2012. Trapping of PARP1 and PARP2 by clinical PARP inhibitors. *Cancer Research* **72**:5588–5599. DOI: https://doi.org/10.1158/0008-5472.CAN-12-2753, PMID: 23118055

Murai J, Huang SY, Renaud A, Zhang Y, Ji J, Takeda S, Morris J, Teicher B, Doroshow JH, Pommier Y. 2014. Stereospecific PARP trapping by BMN 673 and comparison with olaparib and rucaparib. *Molecular Cancer Therapeutics* **13**:433–443. DOI: https://doi.org/10.1158/1535-7163.MCT-13-0803, PMID: 24356813

Pantelidou C, Sonzogni O, De Oliveria Taveira M, Mehta AK, Kothari A, Wang D, Visal T, Li MK, Pinto J, Castrillon JA, Cheney EM, Bouwman P, Jonkers J, Rottenberg S, Guerriero JL, Wulf GM, Shapiro GI. 2019. PARP inhibitor efficacy depends on CD8$^+$ T-cell Recruitment via Intratumoral STING Pathway Activation in BRCA-Deficient Models of Triple-Negative Breast Cancer. *Cancer Discovery* **9**:722–737. DOI: https://doi.org/10.1158/2159-8290.CD-18-1218, PMID: 31015319

Parkes EE, Walker SM, Taggart LE, McCabe N, Knight LA, Wilkinson R, McCloskey KD, Buckley NE, Savage KI, Salto-Tellez M, McQuaid S, Harte MT, Mullan PB, Harkin DP, Kennedy RD. 2017. Activation of STING-Dependent innate immune signaling by S-Phase-Specific DNA damage in breast Cancer. *Journal of the National Cancer Institute* **109**:djw199. DOI: https://doi.org/10.1093/jnci/djw199

Ray Chaudhuri A, Nussenzweig A. 2017. The multifaceted roles of PARP1 in DNA repair and chromatin remodelling. *Nature Reviews Molecular Cell Biology* **18**:610–621. DOI: https://doi.org/10.1038/nrm.2017.53, PMID: 28676700

Rouleau M, Patel A, Hendzel MJ, Kaufmann SH, Poirier GG. 2010. PARP inhibition: parp1 and beyond. *Nature Reviews Cancer* **10**:293–301. DOI: https://doi.org/10.1038/nrc2812, PMID: 20200537

Sen T, Rodriguez BL, Chen L, Corte CMD, Morikawa N, Fujimoto J, Cristea S, Nguyen T, Diao L, Li L, Fan Y, Yang Y, Wang J, Glisson BS, Wistuba II, Sage J, Heymach JV, Gibbons DL, Byers LA. 2019. Targeting DNA damage response promotes antitumor immunity through STING-Mediated T-cell activation in small cell lung Cancer. *Cancer Discovery* **9**:646–661. DOI: https://doi.org/10.1158/2159-8290.CD-18-1020, PMID: 30777870

Shen Y, Rehman FL, Feng Y, Boshuizen J, Bajrami I, Elliott R, Wang B, Lord CJ, Post LE, Ashworth A. 2013. BMN 673, a novel and highly potent PARP1/2 inhibitor for the treatment of human cancers with DNA repair deficiency. *Clinical Cancer Research* **19**:5003–5015. DOI: https://doi.org/10.1158/1078-0432.CCR-13-1391, PMID: 23881923

Shen J, Zhao W, Ju Z, Wang L, Peng Y, Labrie M, Yap TA, Mills GB, Peng G. 2019. PARPi triggers the STING-Dependent immune response and enhances the therapeutic efficacy of immune checkpoint blockade independent of BRCAness. *Cancer Research* **79**:311–319. DOI: https://doi.org/10.1158/0008-5472.CAN-18-1003, PMID: 30482774

Slade D. 2020. PARP and PARG inhibitors in Cancer treatment. *Genes & Development* **34**:360–394. DOI: https://doi.org/10.1101/gad.334516.119, PMID: 32029455

Sun L, Wu J, Du F, Chen X, Chen ZJ. 2013. Cyclic GMP-AMP synthase is a cytosolic DNA sensor that activates the type I interferon pathway. *Science* **339**:786–791. DOI: https://doi.org/10.1126/science.1232458, PMID: 23258413

Swann JB, Smyth MJ. 2007. Immune surveillance of tumors. *Journal of Clinical Investigation* **117**:1137–1146. DOI: https://doi.org/10.1172/JCI31405

Vanpouille-Box C, Alard A, Aryankalayil MJ, Sarfraz Y, Diamond JM, Schneider RJ, Inghirami G, Coleman CN, Formenti SC, Demaria S. 2017. DNA exonuclease Trex1 regulates radiotherapy-induced tumour immunogenicity. *Nature Communications* **8**:15618. DOI: https://doi.org/10.1038/ncomms15618, PMID: 28598415

Vanpouille-Box C, Demaria S, Formenti SC, Galluzzi L. 2018. Cytosolic DNA Sensing in Organismal Tumor Control. *Cancer Cell* **34**:361–378. DOI: https://doi.org/10.1016/j.ccell.2018.05.013

Wang S, Han L, Han J. 2019. Uncoupling of PARP1 trapping and inhibition using selective PARP1 degradation. *Nature Chemical Biology* **15**:1223–1231. DOI: https://doi.org/10.1038/s41589-019-0379-2

Wu X, Wu F-H, Wang X, Wang L, Siedow JN, Zhang W, Pei Z-M. 2014. Molecular evolutionary and structural analysis of the cytosolic DNA sensor cGAS and STING. *Nucleic Acids Research* **42**:8243–8257. DOI: https://doi.org/10.1093/nar/gku569

Wu J, Chen ZJ. 2014. Innate immune sensing and signaling of cytosolic nucleic acids. *Annual Review of Immunology* **32**:461–488. DOI: https://doi.org/10.1146/annurev-immunol-032713-120156, PMID: 24655297

Yum S, Li M, Frankel AE, Chen ZJ. 2019. Roles of the cGAS-STING pathway in Cancer immunosurveillance and immunotherapy. *Annual Review of Cancer Biology* **3**:323–344. DOI: https://doi.org/10.1146/annurev-cancerbio-030518-055636

Zandarashvili L, Langelier MF, Velagapudi UK, Hancock MA, Steffen JD, Billur R, Hannan ZM, Wicks AJ, Krastev DB, Pettitt SJ, Lord CJ, Talele TT, Pascal JM, Black BE. 2020. Structural basis for allosteric PARP-1 retention on DNA breaks. *Science* **368**:eaax6367. DOI: https://doi.org/10.1126/science.aax6367, PMID: 32241924

Zhang Y, Wang J, Ding M, Yu Y. 2013. Site-specific characterization of the asp- and Glu-ADP-ribosylated proteome. *Nature Methods* **10**:981–984. DOI: https://doi.org/10.1038/nmeth.2603

Zhen Y, Yu Y. 2018. Proteomic analysis of the downstream signaling network of PARP1. *Biochemistry* **57**:429–440. DOI: https://doi.org/10.1021/acs.biochem.7b01022, PMID: 29327913

Zitvogel L, Apetoh L, Ghiringhelli F, André F, Tesniere A, Kroemer G. 2008. The anticancer immune response: indispensable for therapeutic success? *Journal of Clinical Investigation* **118**:1991–2001. DOI: https://doi.org/10.1172/JCI35180, PMID: 18523649